The hydraulically smooth limit of flow over surfaces with spanwise heterogeneity

Haosen H.A. Xu [a,*], George I. Park[b], Xiang I.A. Yang[c], Xiaowei Zhu[d]

[a]*Physical Oceanography Laboratory, Ocean University of China, Qingdao, 266005, Shandong, PRC*
[b]*Department of Mechanical Engineering and Applied Mechanics, University of Pennsylvania, Philadelphia, PA 19104, USA*
[c]*Department of Mechanical Engineering, Penn State University, State College, PA 16802, USA*
[d]*Department of Mechanical and Materials Engineering, Portland State University, Portland, OR 97207, USA*

Abstract

Wall slip is conventionally obtained through riblets or grooves. As riblets are macroscopic objects, it is usually not practical to discuss slip patterns at the hydraulically smooth limit. Per Nikuradse, the smooth limit is when the characteristic length of the surface pattern is comparable to the viscous length scale. Recent studies show the possibility of slip at the microscopic scale, making slip patterns at the hydraulically smooth limit relevant. In this study, we leverage a high-fidelity pseudo-spectral code and study flow over surfaces featuring alternating strips of slip and no-slip wall conditions. The wavelength of the surface pattern, denoted as l, varies from 1.5 times the half channel height to 2 viscous units (plus units), eventually approaching the anticipated hydraulically smooth limit. The presence of surface slip gives rise to a slip velocity at the wall, denoted as U_s, which contributes to drag reduction. The surface spanwise heterogeneity leads to secondary flows and intensifies turbulent mixing, consequently leading to drag increase. This drag increase effect can be parameterized using the "roughness function" ΔU^+. The sum of U_s^+ and $-\Delta U^+$ determines whether the surface increases or reduces drag. Here, the superscript + denotes normalization by the wall units. In most cases, the slip velocity at the wall U_s^+ predominates over $-\Delta U^+$, resulting in drag reduction. However, when l is a few viscous units, the roughness function ΔU^+ does not vanish and overwhelms the slip velocity, giving rise to a net drag increase. Considering that the wall is a mixture of slip and no-slip conditions, this drag increase at the anticipated hydraulically smooth limit is unexpected. To gain an insight into the mechanism responsible for this drag increase, we derive a Navier-Stokes-based decomposition of the roughness function. Here, we generalize the definition of the roughness function such that it is a function of the wall-normal coordinate, thereby overcoming the difficulty of measuring the roughness function when the log region is narrow and hard to define. Analysis shows that when l is a few plus units, secondary flows contribute to a slightly positive ΔU^+, while turbulent and viscous contributions, by and large, cancel out, ultimately leading to an overall drag increase at the anticipated hydraulically smooth limit. The evidence in the paper suggests that the hydraulically smooth limit does not exist for certain surfaces.

Keywords: Turbulent boundary layers, Hydraulically smooth limit

1. Introduction

Surfaces exhibiting spanwise heterogeneity are common in both natural environments and fluid engineering applications. In geophysics, such heterogeneity arises from variations in terrain, such as transitions between different canopy types (Belcher et al., 2003; Finnigan et al., 2020). In fluid engineering, spanwise heterogeneity may result from specific manufacturing processes. For instance, additive manufacturing often leads to directional roughness (Altland et al., 2022; Snyder and Thole, 2020). Spanwise heterogeneity in surface patterns as described above gives rise to inhomogeneity in the Reynolds stress, which, in turn, induces secondary flows above them. These secondary flows manifest as alternating high and low momentum pathways in the streamwise-transverse plane and as counter-rotating vortices in the transverse-wall-normal plane (Mejia-Alvarez et al., 2013; Barros and Christensen, 2014; Wangsawijaya et al., 2020). Unlike flow structures identified in the instantaneous flow field (e.g., Adrian, 2007; Yoon et al., 2016; Hong et al., 2011, 2012) that are transient and vanish after taking time average, secondary flows persist in the mean. Furthermore, as the sizes of the secondary flows are often comparable to the boundary-layer height, they can disrupt the log law and the outer layer similarity. Consequently, conventional engineering tools like the Moody diagram, which assumes outer layer similarity and the log law, incur significant uncertainties when applied to surfaces with spanwise heterogeneity (Yang and Anderson, 2018; Medjnoun et al., 2018; Wangsawijaya et al., 2020; Chung et al., 2018). The limitations of existing engineering tools have served as a driving force for research on surfaces with spanwise heterogeneity, and many have contributed to the topic (Vanderwel and Ganapathisubramani, 2015; Modesti et al., 2021; Yang et al., 2019; Forooghi et al., 2020; Yang et al., 2023, to name a few).

An extensively studied configuration involves surfaces with spanwise alternating strips of disparate properties, as sketched in Figure 1. The property may be equivalent roughness height (Willingham et al., 2014; Anderson et al., 2015a), surface topol-

*Corresponding author.
*E-mail address:*xuhaosen@ouc.edu.cn

Symbols		$\Delta U^+_{b,d}$	Dispersive contribution to ΔU^+_b
B	Canonical log-law intercept	Δx	Grid spacing in the streamwise direction
C	Log-law intercept	Δy	Grid spacing in the wall-normal direction
C_f	Skin friction	Δz	Grid spacing in the spanwise direction
F_b	Body force	κ	Von Kármán Constant
H	Size of the secondary flow structure	ρ	Density
l	Wavelength of the spanwise heterogeneity	τ	Shear stress
l_{slp}	Size of the slip strip	τ_R	Reynolds stress
l_{nslp}	Size of the no-slip strip	τ_D	Dispspersive stress
L	Streamwise domain size	τ_v	Viscous stress
N	Grid number	ν	Kinematic viscosity
n	Wall-normal direction		
k	Roughness height	*Abbreviations*	
Re_τ	Friction Reynolds number	WMLES	Wall-modeled large eddy simulation
u	Streamwise velocity	DNS	Direct numerical simulation
u_τ	Friction velocity		
$\mathbf{u}$	Velocity vector	*Superscripts, Subscripts, & Operators*	
$\mathbf{u_h}$	Horizontal velocity vector	$(\cdot)^+$	Normalization by wall units
$\mathbf{u_n}$	Normal velocity component	$(\cdot)^+_b$	Normalization by bottom wall units
U	Double-averaged streamwise velocity	$(\cdot)'$	Temporal fluctuation of $(\cdot)$
U_{bulk}	Bulk velocity	$(\cdot)''$	Spatial variation of $(\cdot)$
U_s	Slip velocity	$(\cdot)_b$	$(\cdot)$ at the bottom wall
v	Wall-normal velocity	$(\cdot)_c$	$(\cdot)$ at the top wall
w	Spanwise velocity	$(\cdot)_i$	$(\cdot)$ in the *ith* direction
x	Streamwise coordinate	$(\cdot)_{pc}$	$(\cdot)$ in a plane channel
y	Wall-normal coordinate	$(\cdot)_{nslp}$	$(\cdot)$ at the no-slip region
z	Spanwise coordinate	$(\cdot)_{slp}$	$(\cdot)$ at the slip region
		$(\cdot)_t$	$(\cdot)$ at the top wall
Greek Symbols		$(\cdot)_w$	$(\cdot)$ at the wall
δ	Boundary layer height	$(\cdot)_x$	$(\cdot)$ in the streamwise direction
δ_{ij}	Kronecker delta	$(\cdot)_y$	$(\cdot)$ in the wall-normal direction
ΔU	Roughness function	$(\cdot)_z$	$(\cdot)$ in the spanwise direction
$\Delta U^+_{b,v}$	Viscous contribution to ΔU^+_b	$\bar{(\cdot)}$	Temporal average
$\Delta U^+_{b,r}$	Turbulence contribution to ΔU^+_b	$\langle(\cdot)\rangle$	Spatial average

Table 1: Nomenclature Table

ogy (García-Mayoral and Jimenez, 2011; Vanderwel and Ganapathisubramani, 2015; Modesti et al., 2021), wall-shear stress (Chung et al., 2018), heat flux (Salesky et al., 2022), and slip length (Neuhauser et al., 2022). Among the numerous parameters influencing surface properties, the wavelength of the spanwise heterogeneity, denoted as l, has garnered considerable attention. Yang and Anderson (2018) varied the wavelength of the spanwise heterogeneity from $l/\delta = 0.1$ to 2π, where δ is the outer length scale, corresponding to boundary-layer height, half channel height, or pipe radius depending on the flow. Three regimes were identified: the roughness regime for small l/δ, the topography regime for large l/δ, and the intermediate regime that lies between the roughness regime and the topography regime. In the roughness regime, the sizes of the secondary flows are small compared to the boundary-layer height, and the outer-layer similarity survives. Conversely, in the topography regime, the sizes of the secondary flows are comparable to the boundary-layer height, precluding outer-layer similarity. The impact of the secondary flows on the surface drag depends on their sizes and locations. Large-scale secondary flows enhance

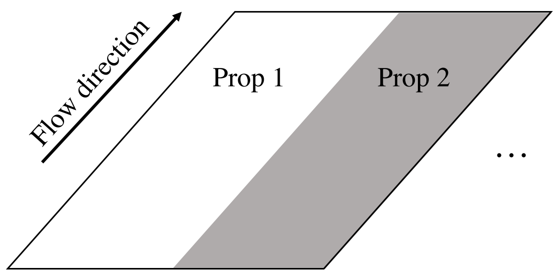

Figure 1: Schematic of flow over surfaces with spanwise alternating strips of disparate properties.

mixing and therefore increase drag (Choi et al., 1993; Suzuki and Kasagi, 1994). Small-scale secondary flows, e.g., those above riblets, push coherent streamwise vortices away from the wall, thereby reducing the drag force (Choi et al., 1993; Martin and Bhushan, 2016; Wong et al., 2024).

An anticipated limit is when l is very small. As l approaches a few viscous units, the relevant length scale becomes the viscous length scale ν/u_τ. Here, ν is the kinematic viscosity, and u_τ is the friction velocity. For rough-wall boundary-layer flows, this defines the hydraulically smooth limit (Schlichting et al., 1980): when the characteristic length scale of the surface roughness is comparable to the viscous length scale, the surface roughness is fully submerged within the viscous sublayer. It is worth noting that the hydraulically smooth limit does not concern the surface coverage density. In Nikuradse's experiment, the hydraulically smooth limit is obtained when the entire surface is still covered by sandgrain roughness. For flow over regular roughness, e.g., cubes and spheres, the hydraulically smooth limit can be obtained for arbitrary surface coverage densities. At this hydraulically smooth limit, the flow behaves like a smooth-wall boundary layer: the mean flow adheres to the well-established law of the wall while maintaining the outer-layer similarity. The concept of the hydraulically smooth limit was first established in the seminal works of Nikuradse (1933) and Schlichting and Gersten (1979). More recently, Flack et al. (2012) revisited this concept. In these studies, the roughness is homogeneous, for which the roughness height k serves as a good characteristic length scale. Schlichting and Gersten (1979) found that the hydraulically smooth limit is when $k^+ < 4$. Flack et al. (2012), on the other hand, found that roughness geometry can influence the critical k^+ value for the hydraulically smooth behavior, with certain surfaces remaining hydraulically smooth up to $k^+ = 10$.

In the context of surfaces with spanwise heterogeneity, the roughness height is not always defined, and l becomes the characteristic length scale of the surface structure. This is a common practice in wall-modeled large-eddy simulations (WMLES) where roughness is often parametrized using an equivalent roughness height y_0 without introducing k/δ as a parameter (Bose and Park, 2018; Yang et al., 2017). The practice is sometimes adopted in DNS, where roughness is not explicitly resolved, and a shear stress boundary condition is instead imposed (Chung et al., 2018; Neuhauser et al., 2022). Thus, the presumed hydraulically smooth limit is when l^+ is $O(1)$. The primary objective of this work is to study the flow as the surface roughness approaches this anticipated hydraulically smooth regime. In particular, we will focus specifically on the flow above surfaces featuring alternating strips of slip and no-slip regions. We note that a slip wall is commonly used to model the interaction between a superhydrophobic surface and a fluid flow (Martell et al., 2009, 2010; Park et al., 2013; Türk et al., 2014). The boundary condition could correspond to a surface with streamwise aligned micro wedges (Park et al., 2013; Türk et al., 2014; Jelly et al., 2014), where air is trapped between two neighboring wedges, leading to a slip condition there. This is well established and recent papers that adopt a slip condition rarely compare against experiments (Türk et al., 2014; Jelly et al., 2014).

From a practical standpoint, slip patterns at such a scale are unimaginable as conventional methods generate slip via riblets or grooves, whose sizes are usually significantly larger than the viscous scale (Bechert et al., 1997; García-Mayoral and Jimenez, 2011; Endrikat et al., 2021). Recent research has shown a wall-shear-stress-dependent slip at the molecular scale, making slip patterns at viscous length scales relevant (Thompson and Troian, 1997; Yong and Zhang, 2013; Ramos-Alvarado et al., 2016). As this paper focuses on fluid dynamics, a more in-depth discussion of molecular dynamics is outside the scope of this paper, and the reader is directed to the references cited above for further details.

In a numerical simulation, the no-slip region is a region with a Dirichlet boundary condition $\mathbf{u} = 0$ (assuming a stationary wall), while the slip region is a region with a Neumann and no-penetration boundary conditions, i.e., $\partial \mathbf{u_h}/\partial n = 0, \mathbf{u_n} = \mathbf{0}$. The relevant length scales in this case are the viscous length scale or the plus unit ν/u_τ, the outer length scale δ, and the wavelength of the surface pattern l. In this study, we will vary the wavelength of the pattern from 1.5 δ to 2 plus units. While we vary the wavelength, the overall configuration remains unchanged, and 50% of the surface is always free-slip. Again, the hydraulically smooth limit concerns the characteristic length scale of the surface pattern and does not concern the surface coverage density.

While not the focus of this study, the flow over superhydrophobic surfaces bears direct relevance. Superhydrophobic surfaces are surfaces with microstructures that trap air (Carré and Mittal, 2009). One such microstructure is microgrooves that trap air between two ridges. Unlike drag reduction by microgrooves(Lee and Lee, 2001) and spanwise jet forcing (Yao et al., 2018; Nozarian et al., 2024), which lifts turbulent vortices from the wall, the trapped air prevents water from direct contact with the solid surface, leading to a slip at the air-water interface. When the microgrooves are aligned in the direction of the flow, the surface can be modeled as alternating free-slip and no-slip strips, which is the configuration considered in this work. Many prior computational studies have also focused on this configuration (Martell et al., 2009, 2010; Park et al., 2013; Türk et al., 2014; Jelly et al., 2014; Tomlinson et al., 2023). Given the relevance of these studies to our work, we provide a brief review of that literature here. Martell et al. (2009, 2010) demonstrated that $U - U_s$ (difference between the mean velocity and the slip velocity) exhibits similar behavior as U above a no-slip wall as they both have a viscous sublayer ($U^+ - U_s^+ = y^+$) and a logarithmic layer ($U^+ - U_s^+ = \ln(y^+)/\kappa + C$). Here, U_s^+ represents the slip velocity at the wall, and the value of C depends on the specific surface. Türk et al. (2014) varied the wavelength from $l = \pi\delta$ to $l^+ = 8.8$, a length scale close to the focus of this study, and reported drag reduction in all their DNS results. They found that the slip length defined as $U_s/(dU/dn)_w$ increases with l, where $(\cdot)_w$ denotes the flow variable $(\cdot)$ at the wall. They also noted that the laminar solution provides a reasonable approximation for the slip length when $l^+ \lesssim 20$. Jelly et al. (2014) conducted a budget and integral analysis for a specific wavelength of $l^+ = 67.5$. Their findings suggested that while the surface reduces drag, the no-slip region experiences higher skin friction. This increased skin friction is a consequence of diffusion, which transports high-momentum fluid from above the slip region to above the no-slip region. Tomlinson et al. (2023) took a further step and studied the effects of surfactants in drag reduction of superhydrophobic surfaces. Due to the existence of surfactants, they modeled the superhydrophobic surfaces as long but finite-length alternating streamwise strips of constant Maragoni shear rate and no-slip boundary conditions.

Although the limit of $l \to 0$ had not been the focus of any prior study on superhydrophobic surfaces due to a lack of practicality, there is an expectation for the mean flow when $l \to 0$. Below, we review these expectations. Firstly, it is anticipated that the log layer will survive (Martell et al., 2010; Jelly et al., 2014). The mean flow is expected to follow

$$U^+ - U_s^+ = \frac{1}{\kappa}\ln(y^+) + B - \Delta U^+ \quad (1)$$

in the log layer, where U_s^+ is the slip velocity at the wall, $B \approx 5$, and ΔU^+ is analogous to the "roughness function". Note that the roughness function is obtained by comparing against a flat-plate boundary layer at the same Reynolds number, whereas ΔU^+ defined here is obtained by comparing against the log law $\ln(y^+)/\kappa + B$. Secondly, from Martell et al. (2009) and Martell et al. (2010), it is expected that U_s^+ is an increasing function of l^+, with $U_s^+ - \Delta U^+$ being positive for all values of l^+. Thirdly, from Türk et al. (2014), it is anticipated that the roughness function ΔU^+ is an increasing function of l^+, and $\Delta U^+ = 0$ when $l^+ = 0$. Lastly, it is expected that turbulent mixing/diffusion will contribute positively to ΔU^+, while secondary flows should contribute negatively to ΔU^+ — at least for some l^+ values (Jelly et al., 2014). In the following section, we will study the behaviors of the flow as l^+ approaches $O(1)$ and put the above expectations to the test.

In anticipation of the discussion in the following sections, we make mention of the two analysis tools. The first tool is the triple decomposition of the velocity, which separates the instantaneous velocity into the double-averaged component, the variations of the time average in space, and the fluctuation in time:

$$u = U + u' + \bar{u}'', \quad (2)$$

where U is the double-averaged velocity, i.e., $\langle \bar{u} \rangle$. $\bar{(\cdot)}$ denotes time averaging and $\langle\cdot\rangle$ denotes wall-parallel averaging. $(\cdot)'$ and $(\cdot)''$ denote the fluctuation in time and the variation in space. The second tool is the integral method (Fukagata et al., 2002; Renard and Deck, 2016; Volino and Schultz, 2018; Elnahhas and Johnson, 2022). The integral methods in these references provide a decomposition of the skin friction coefficient. Türk et al. (2014) adapted the method and analyzed the flow rate. In our study, we will adapt the integral method to investigate the roughness function ΔU^+.

The rest of the paper is organized as follows. We elaborate on the expected mean flow behavior in §2. The details of our DNSs are presented in §3 with the results in §4. In §5, we discuss the effect of spanwise slip. Finally, we conclude in §6.

2. The anticipated mean flow behavior

In this section, we elaborate on the expected behaviors of the mean flow above a surface with spanwise heterogeneity featuring alternating strips of slip and no-slip regions as sketched in Figure 1 as l varies. When l is much larger than δ, spanwise heterogeneity affects the flow near the interfaces of two neighbouring patches only, and the mean flow is approximately spanwise homogeneous above each individual patch. The flow above the no-slip-wall patch is given by the law of the wall and is approximately

$$\frac{U_{\text{nslp}}}{\sqrt{\tau_{w,\text{nslp}}/\rho}} = \frac{1}{\kappa}\ln\left(\frac{y\sqrt{\tau_{w,\text{nslp}}/\rho}}{\nu}\right) + B. \quad (3)$$

The slip wall applies no force on the flow, and therefore the mean flow above the slip-wall patch is approximately

$$U_{\text{slp}} = \text{Const.} \quad (4)$$

Here, the subscripts "nslp" and "slp" stand for "no-slip" and "slip", τ_w is the wall-shear stress, and ρ is the fluid density. The double-averaged velocity is given by

$$U = \frac{l_{\text{nslp}} U_{\text{nslp}} + l_{\text{slp}} U_{\text{slp}}}{l_{\text{nslp}} + l_{\text{slp}}}, \quad (5)$$

in the log layer, which leads to

$$U = (U_{\text{nslp}} + U_{\text{slp}})/2, \quad (6)$$

since $l_{\text{nslp}} = l_{\text{slp}}$. The wall-shear stress is given by

$$\tau_w = \frac{l_{\text{nslp}}\tau_{w,\text{nslp}} + l_{\text{slp}}\tau_{w,\text{slp}}}{l_{\text{nslp}} + l_{\text{slp}}} = 0.5\tau_{w,\text{nslp}}. \quad (7)$$

It follows from (3), (4), (6), and (7) that the mean flow in the log layer is

$$U^+ = \frac{U}{\sqrt{\tau_w/\rho}} \approx U_s^+ + \frac{0.71}{\kappa}\ln(y^+) + 4.2. \quad (8)$$

Alternatively,

$$U^+ - U_s^+ = \frac{0.71}{\kappa}\ln(y^+) + B - \Delta U^+, \text{ with } \Delta U^+ \approx 0.8. \quad (9)$$

Here, typical values for $\kappa = 0.4$ and $B = 5$ are invoked. ΔU^+ as defined here is analogous to the roughness function. Equation (9) suggests a logarithmic scaling with a smaller log-law slope and a smaller additive constant than the law of the wall.

When l is comparable to the half channel height, secondary motions would occupy the entire outer layer, and it is hard to estimate the mean flow, at least theoretically (Anderson et al., 2018; Hansen et al., 2023). Nonetheless, empirical evidence seems to support the following mean flow scaling

$$U^+ - U_s^+ = \frac{1}{\kappa}\ln(y^+) + B - \Delta U^+, \quad (10)$$

for $\nu/u_\tau \ll y \ll \delta$. In most studies, the slip velocity $U_s = 0$. It is worth noting that due to spanwise heterogeneity, log layer

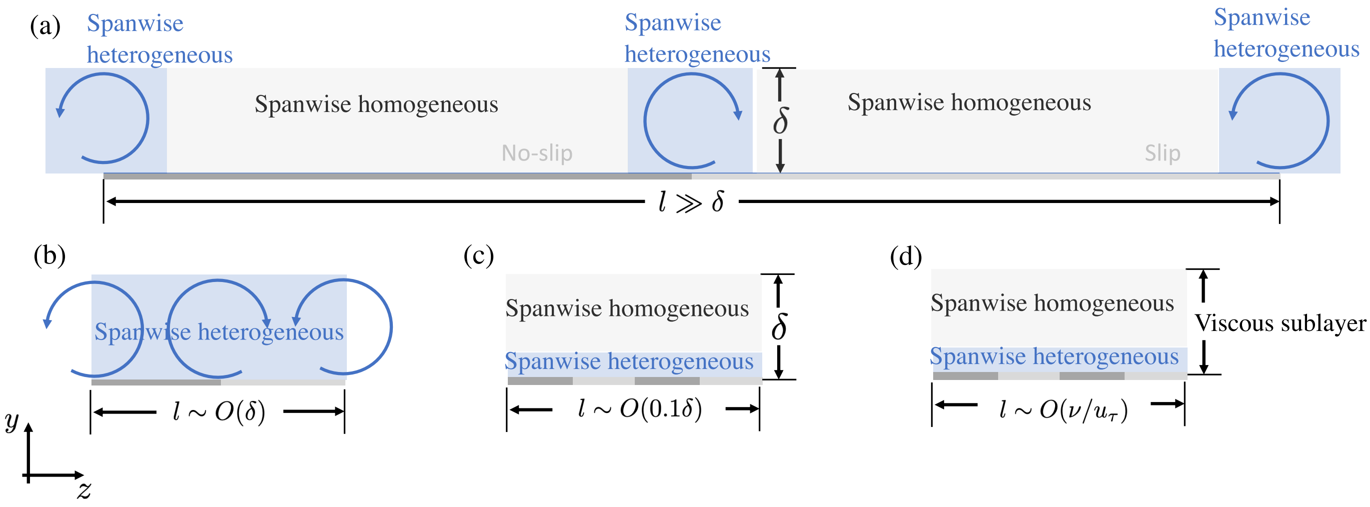

Figure 2: A sketch of the flow as the spanwise length scale of the surface varies.

in its conventional sense does not exist, and (10) can only be regarded as a fortuitous working approximation.

Further decreasing l to $O(0.1\delta)$, the height of the resulting secondary motions becomes sufficiently small and a logarithmic layer in its conventional sense can exist. As a result, the mean flow follows (10). In this regime, the spanwise heterogeneity in the surface's property can already be regarded as roughness.

Last, when l is comparable to the viscous scale, spanwise heterogeneity in the mean flow would be confined within the viscous sublayer, and the surface is expected to be hydraulically smooth. Consequently, a log layer in its conventional sense exists, and the mean flow there is

$$U^+ = \frac{1}{\kappa}\ln(y^+) + B. \tag{11}$$

The slip velocity $U_s = 0$, and the roughness function $\Delta U^+ = 0$.

Figure 2 is a sketch of the flow as the spanwise length scale of the surface varies. Spanwise heterogeneity with $l \gtrsim O(0.1\delta)$ has received considerable attention. We will focus on the regime where $l \sim O(\nu/u_\tau)$.

3. Computational Details

We solve the following incompressible Navier-Stokes equations in a periodic channel

$$\frac{\partial u_j}{\partial x_j} = 0, \tag{12}$$

$$\frac{\partial u_i}{\partial t} + u_j\frac{\partial u_i}{\partial x_j} = -\frac{\partial p}{\partial x_i} + \nu\frac{\partial^2 u_i}{\partial x_j \partial x_j} + F_b\delta_{i1}, \tag{13}$$

where u_i is the velocity in the ith Cartesian direction. The fluid density $\rho \equiv 1$ and is dropped. Figure 3 is a sketch of the flow configuration. The configuration is a channel, and the half-channel height is δ. A constant body force F_b drives the flow in the streamwise direction. Define the bulk friction velocity

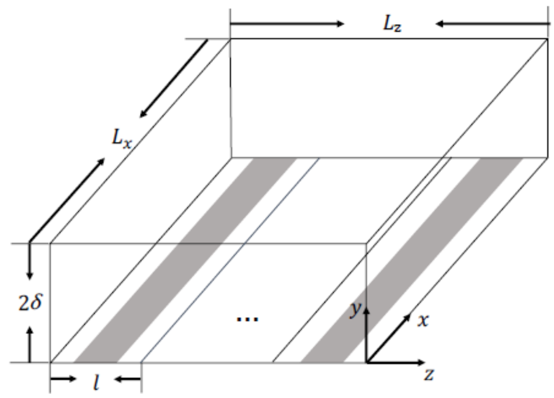

Figure 3: A sketch of the flow configuration. The top wall is smooth. The bottom wall features spanwise alternating strips of slip and no-slip conditions. l is the size of the repeating unit in the spanwise direction.

as $u_\tau = \sqrt{F_b\delta}$. The bulk friction Reynolds number defined as $Re_\tau = u_\tau\delta/\nu$ is 180 for all cases. Note that since the focus of this study is the hydraulically smooth regime, flows at low Reynolds numbers are more relevant than flows at high Reynolds numbers. The top wall is a no-slip, no-penetration one. The bottom wall features alternating strips with slip and no-slip conditions. Two types of slip conditions are investigated:

$$\frac{\partial u}{\partial n} = 0, \;\; \frac{\partial w}{\partial n} = 0, \tag{14}$$

which imposes slip for both the streamwise and the spanwise velocity, and

$$\frac{\partial u}{\partial n} = 0, \;\; w = 0, \tag{15}$$

which imposes slip for the streamwise velocity and no-slip for the spanwise velocity. Here, n is the wall-normal (y) direction, u and w are the velocity in the streamwise (x) and the spanwise (z) directions. We vary the spanwise length scale l from 1.5δ to $2.1\nu/u_\tau$, whilst keeping $l_{\mathrm{slp}} = l_{\mathrm{nslp}}$. Although symmetric wall

Case	Re_τ	l^+_{slp}	l^+_{nslp}	$L_x \times L_y \times L_z(\delta)$	$N_x \times N_y \times N_z$	Δx^+	Δy^+_w	Δy^+_c	Δz^+
R2	180	135.00	135.00	$6 \times 2 \times 3$	$128 \times 128 \times 576$	8.44	0.35	5.00	0.94
LL2	180	135.00	135.00	$9 \times 2 \times 4.5$	$192 \times 128 \times 864$	8.44	0.35	5.00	0.94
L2	180	135.00	135.00	$12 \times 2 \times 6$	$256 \times 128 \times 1152$	8.44	0.35	5.00	0.94
R4	180	67.50	67.50	$6 \times 2 \times 3$	$128 \times 128 \times 576$	8.44	0.35	5.00	0.94
X4	180	67.50	67.50	$6 \times 2 \times 3$	$128 \times 128 \times 576$	8.44	0.35	5.00	0.94
R8	180	33.75	33.75	$6 \times 2 \times 3$	$128 \times 128 \times 576$	8.44	0.35,	5.00	0.94
L8	180	33.75	33.75	$12 \times 2 \times 3$	$256 \times 128 \times 576$	8.44	0.35	5.00	0.94
M8	180	33.75	33.75	$6 \times 2 \times 3$	$128 \times 128 \times 128$	8.46	0.35	5.00	4.22
R16	180	16.88	16.88	$6 \times 2 \times 3$	$128 \times 128 \times 576$	8.44	0.35	5.00	0.94
X16	180	16.88	16.88	$6 \times 2 \times 3$	$128 \times 128 \times 576$	8.44	0.35	5.00	0.94
R32	180	8.44	8.44	$6 \times 2 \times 3$	$128 \times 128 \times 640$	8.44	0.35	5.00	0.84
R64	180	4.22	4.22	$6 \times 2 \times 3$	$128 \times 128 \times 768$	8.44	0.35	5.00	0.70
R128	180	2.11	2.11	$6 \times 2 \times 3$	$128 \times 128 \times 1024$	8.44	0.35	5.00	0.53
X128	180	2.11	2.11	$6 \times 2 \times 3$	$128 \times 128 \times 1024$	8.44	0.35	5.00	0.53
R256	180	1.05	1.05	$6 \times 2 \times 3$	$128 \times 128 \times 1024$	8.44	0.35	5.00	0.53

Table 2: DNS details. l_{slp} and l_{nslp} are the spanwise sizes of the slip and no-slip strips. Δy^+_w and Δy^+_c are the grid resolution at the wall and the channel centerline, respectively.

boundary conditions were used (Park et al., 2013; Türk et al., 2014; Jelly et al., 2014), the use of asymmetric wall boundary conditions is also common (Martell et al., 2009, 2010). In the present study, the asymmetric wall boundary condition is adopted. Hence, the flow is asymmetric with respect to the channel centerline due to the disparate wall conditions on the top and bottom walls. For the DNSs in this study, $\tau_{w,b}$ ranges from 0.74 to 1.02 $F_b\delta$, and $\tau_{w,t}$ ranges from 1.26 to 0.98 $F_b\delta$. Here, the $\tau_{w,b}$ and $\tau_{w,t}$ are the mean bottom and top wall shear stresses, and $\tau_{w,b} + \tau_{w,t} = 2F_b\delta$ due to force balance. The asymmetric wall boundary condition makes it easier to quantify the drag increase/reduction of the bottom wall with respect to the top wall. This will be discussed further in §4.

The size of the computational domain is $L_x \times L_y \times L_z = 6\delta \times 2\delta \times 3\delta$. When scaled in mean wall units, i.e., ν/u_τ, the present computational domain is comparable to the ones in Martell et al. (2009), Martell et al. (2010), and Park et al. (2013), and is larger than the ones in Rastegari and Akhavan (2015), and the minimal span channel in MacDonald et al. (2017). To further validate the adequacy of the present domain size, we include a domain convergence study in §Appendix A. We shall see that the present domain is sufficient. The grid is uniform in the streamwise and the spanwise directions, respectively, and is stretched according to a hyperbolic tangent function in the wall-normal direction. The resolution is such that $\Delta x^+ \approx 8.5$ in the streamwise direction, $\Delta z^+ < 1$ in the spanwise direction except M8, $\Delta y^+_w \approx 0.35$ at the wall, and $\Delta y^+_c \approx 5.0$ at the channel centerline. A grid convergence study for the aforementioned mesh settings could be found in Türk et al. (2014). There, it was reported that coarse spanwise grid resolution causes overestimates of drag reduction or underestimates of the wall-shear stress. Hence, when a drag increase is predicted, the prediction is going to be conservative. Turbulence gives rise to flow intermittency, and higher-order statistics will require finer grid resolutions (Chen et al., 2023; Yang et al., 2021). This study focuses on first- and second-order statistics. For these statistics, the present grid resolution should be sufficient (Moser et al., 1999; Min and Kim, 2004; Jelly et al., 2014).

Further details of the DNSs are summarized in Table 2. The nomenclature of the baseline DNSs is R[L_z/l]. In R[L_z/l], we impose the slip condition for both the streamwise and the spanwise velocities, i.e., the condition in (14). In X[L_z/l], we impose the slip condition for the streamwise velocity and the no-slip condition for the spanwise velocity, i.e., the condition in (15). To verify the adequacy of the domain size, cases LL2 and L2 are the same as R2 but with their domain sizes 1.5 times and 2 times of that in R2 in both the streamwise and the spanwise direction. In addition, case L8 is the same as R8 but with its streamwise domain size 2 times that of R8. For further validation of the DNS code, case M8 is a replication of the "$30\mu m - 30\mu m$" case in Martell et al. (2009). The averaging time is such that $t \geq 2000 L_x/U_{bulk}$ after the flow reaches a statistically stationary state, with U_{bulk} being the bulk streamwise velocity. This averaging time is longer than most DNS studies in the literature (Coceal et al., 2006; Yuan and Piomelli, 2014; Chung et al., 2018; Ma et al., 2021; Zhang et al., 2023). The adequacy of the averaging time is further verified in §Appendix A, where we compared the computed momentum budget to the known analytical solution.

We employ the open-source pseudo-spectral code JHU-LESGO (2019) for our DNSs. The code solves the incompressible Navier-Stokes equations in a periodic channel. It uses a pseudo-spectral method in the wall-parallel directions and a second-order finite difference method in the wall-normal direction, respectively. Time marching uses a second-order Adam-Bashforth method. The code has been extensively validated and has previously been used for boundary-layer flow calculations (Bou-Zeid et al., 2005; Chester et al., 2007; Anderson et al., 2015b; Yang et al., 2015; Zhang et al., 2022). In addition, the pseudo-spectral method has also been extensively validated for simulating turbulent flows over surfaces with abrupt changes in properties (García-Mayoral and Jimenez, 2011; García-Mayoral and Jiménez, 2012; Fairhall and García-Mayoral, 2018; Fairhall et al., 2019), which are similar to the flow configuration in the present study. Further details of the code can be found in Altland et al. (2022) and are not recaptured here for brevity.

4. Results

We present the DNS results of the baseline R cases. We will establish a drag increase at the anticipated hydraulically smooth limit in §4.1. Recognizing the limited size of the logarithmic region and the associated difficulty and uncertainty in defining the “roughness function”, a Navier-Stokes-based decomposition is derived in §4.2, focusing on the difference between the present flow and the flow above a smooth wall. The analysis will show that the secondary flows are responsible for the observed drag increase. Further analysis of the secondary flows is presented in §4.3, where we will show the flow above slip-wall regions is the culprit of the drag increase.

4.1. Mean flow

Figure 4 (a) shows the mean velocity profiles U_b^+ as a function of y_b^+ for the R cases. Here, the subscript b signifies normalization by the friction velocity at the bottom wall. Profiles are truncated at the top where the Reynolds shear stress $\langle \overline{u'v'} \rangle$ equals 0, beyond which the flow is more influenced by the top wall than the bottom wall. A noticeable non-zero slip velocity at the wall is observed. Figure 4 (c) shows the slip velocity as a function of the spanwise length scale l_b^+. Again, the subscript b denotes normalization by the wall units measured at the bottom wall. We see that the slip velocity is an increasing function of l_b^+, which is consistent with §2. The slip velocity approaches 0 as l_b^+ approaches 0. Figure 4 (b) displays $U_b^+ - U_{s,b}^+$ as a function of y_b^+. The plane channel result is included for comparison purposes. A universal viscous sublayer is found, and all profiles collapse for $y^+ < 2$. This is again consistent with §2. A log region can be identified in profiles although the log law intercepts vary. Hereby we obtain the log-law slope and the corresponding intercepts by fitting U_b^+ as a function of $\ln(y_b^+)$ between $y_b^+ = 50$ and 80. In Figure 4 (d), ΔU_b^+, the deviation from the smooth-wall log law intercept, is shown as a function of l_b^+. The value of ΔU_b^+ increases from -1.43 in R2 to 1.73 in R8, and subsequently decreases from 1.73 in R8 to 0.75 in R256 as l_b^+ decreases from 63.9 to 2.13. Notably, ΔU_b^+ remains non-zero in R256 when $l_b^+ \sim O(1)$, in the anticipated hydraulically smooth limit.

Upon closely examining the results in Figure 4 (b), we observe that the R2 profile exhibits a different log-law slope. The results for the log-law slope are presented in Figure 5. The log law slope in R2 is notably different from the other cases at similar Reynolds numbers. Hence, the deviation of the log law slope in R2 from the canonical value cannot be attributed to the low Reynolds number. Our argument in §2 might explain the deviation of the log law slope in R2 from the canonical value. In fact, the measured log-law slope in R2 is 2.04, which is reasonably close to $0.71/\kappa$, the log-law slope in (9).

The slip velocity arises from the presence of the slip wall, and it contributes to drag reduction. The modified roughness function ΔU_b^+, on the other hand, is a result of spanwise heterogeneity in the surface roughness, and it contributes to drag

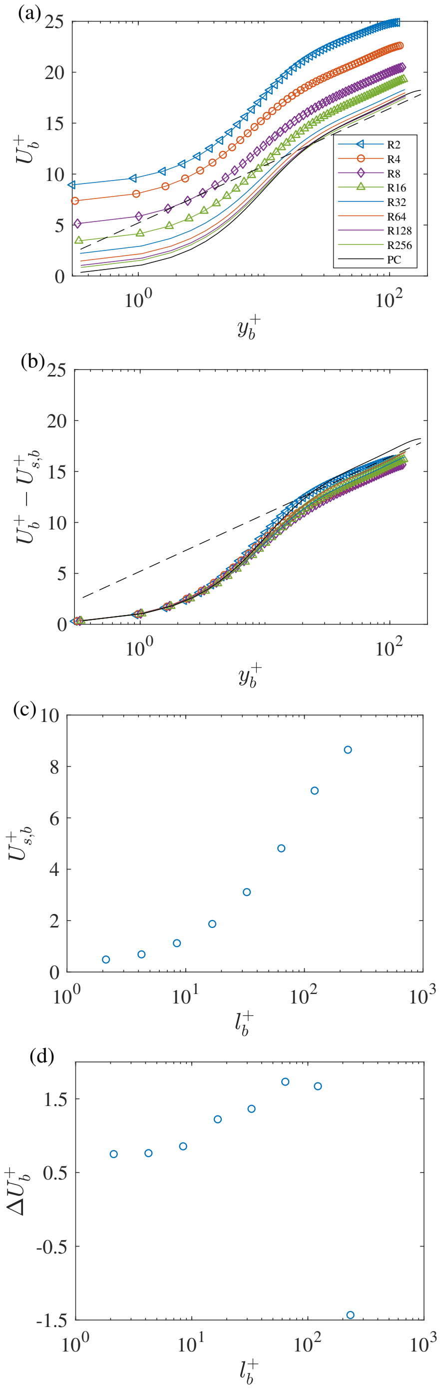

Figure 4: (a) Mean velocity profiles as a function of the wall-normal coordinate. The plane channel result is included for reference and is denoted as PC. The dashed line corresponds to the log law with $\kappa = 0.41$ and $B = 5.2$. (b) Same as (a) but with the slip velocities subtracted from the mean velocity profile. (c) Slip velocities as a function of the spanwise length scale l_b^+. (d) Roughness function as a function of the spanwise length scale l_b^+. Here, the subscript b denotes normalization based on the friction velocity at the bottom wall.

increase. The two mechanisms compete and determine if the surface reduces or increases drag. Figure 6 (a) shows $U_{s,b}^+ - \Delta U_b^+$ as a function of l_b^+. Again, the subscript b denotes normalization by the wall units measured at the bottom wall. The value of $U_{s,b}^+ - \Delta U_b^+$ is positive in cases R2 to R64, leading to drag

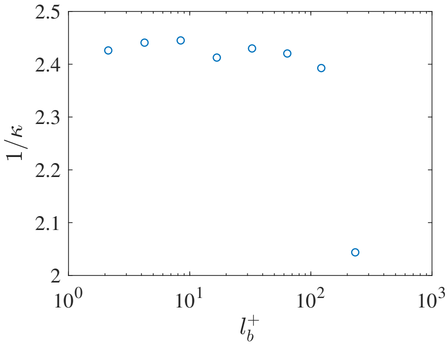

Figure 5: The measured log-law slopes, i.e., $1/\kappa$ as a function of the spanwise length scale. The value $1/\kappa$ for the canonical plane channel is marked by the dashed line.

reduction in these cases. Similar drag reduction was observed in previous studies such as Martell et al. (2009) and Türk et al. (2014). The value of $U_{s,b}^+ - \Delta U_b^+$ decreases as l_b^+ decreases, which is consistent with the discussion in §2. However, what defies expectations is the slightly negative values of $U_{s,b}^+ - \Delta U_b^+$ in cases R128 and R256. As l_b^+ approaches 0, $U_{s,b}^+ - \Delta U_b^+$ should approach 0 as well, if not slightly positive. This drag increase is more clear in Figure 6 (b), where we show $\tau_{w,b}/u_\tau^2$ as a function of l_b^+. According to force balance, $\tau_{w,b}/u_\tau^2 + \tau_{w,t}/u_\tau^2 = 2$. In the cases of a smooth top wall, $\tau_{w,b}/u_\tau^2 > 1$ indicates drag increase on the bottom wall, whereas $\tau_{w,b}/u_\tau^2 < 1$ suggests drag reduction. Here, we observe that $\tau_{w,b}/u_\tau^2$ surpasses 1 in cases R128 and R256, signifying drag increase in these instances. In addition, Figure 6 (c) shows that the bulk velocity in drag increase instances decreases below the plane channel result even though the slip velocity is non-zero. Consequently, the skin friction coefficient, defined as $C_f = \tau_w/\left(\rho U_{bulk}^2/2\right)$ increases above the plane channel result in those instances, as shown in Figure 6 (d).

4.2. *A decomposition of the generalized roughness function*

In this section, we study what might be responsible for the drag increase in R128 and R256. We begin by defining the generalized roughness function ΔU_b^+ as follows:

$$\Delta U_b^+ = -(U_b^+ - U_{s,b}^+) + U_{\text{pc}}^+, \tag{16}$$

where U_{pc}^+ is the velocity from the plane channel, and the subscript "pc" stands for "plane channel". Again, the subscript b denotes normalization by the friction velocity at the bottom wall. Equation (16) is a straightforward extension of (10): the generalized roughness function ΔU_b^+ in (16) exists in the sublayer, the log layer, and the wake layer, whereas ΔU_b^+ in (10) exists only in the log layer. Thus defined ΔU_b^+ overcomes the difficulty in measuring the roughness function when the log region is narrow and not well defined.

We proceed with deriving a decomposition for the generalized roughness function ΔU_b^+. Beginning with the double-averaged Navier-Stokes equation in a channel, we have:

$$\frac{d\left\langle \overline{u'v'}\right\rangle}{dy} + \frac{d\left\langle \overline{u}''\overline{v}''\right\rangle}{\partial y} = F_b + \nu\frac{d^2\left\langle \overline{u}\right\rangle}{d^2 y}, \tag{17}$$

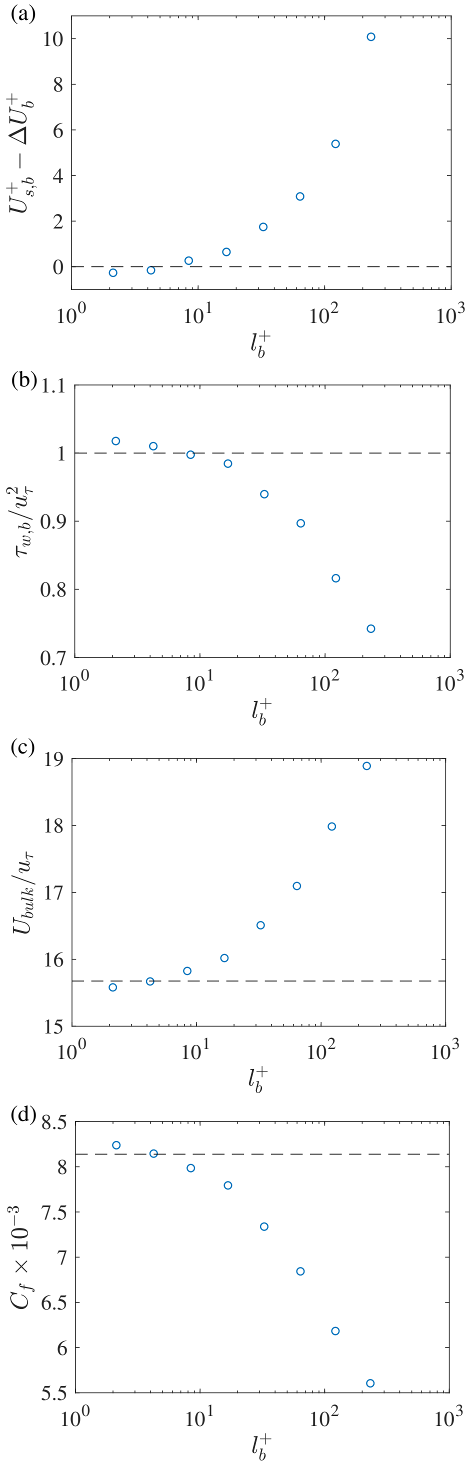

Figure 6: (a) $\Delta U_b^+ - U_{s,b}^+$ as a function of l_b^+. (b) Bottom wall-shear stress normalized by bulk friction velocity. (c) Bulk velocity. (d) Skin friction coefficient. The plane channel results are marked by the dashed lines.

with the mean convective term being zero. For a plane channel, $Re_\tau = Re_{\tau,b}$, and integrating (17) twice in the wall-normal direction leads to

$$\bar{u}_{pc}^+ = \left(-\frac{1}{2Re_\tau}y_b^{+2} + y_b^+\right) + \int_0^{y_b^+} \overline{u'v'}_{\text{pc}}^+ d\tilde{y}_b^+. \tag{18}$$

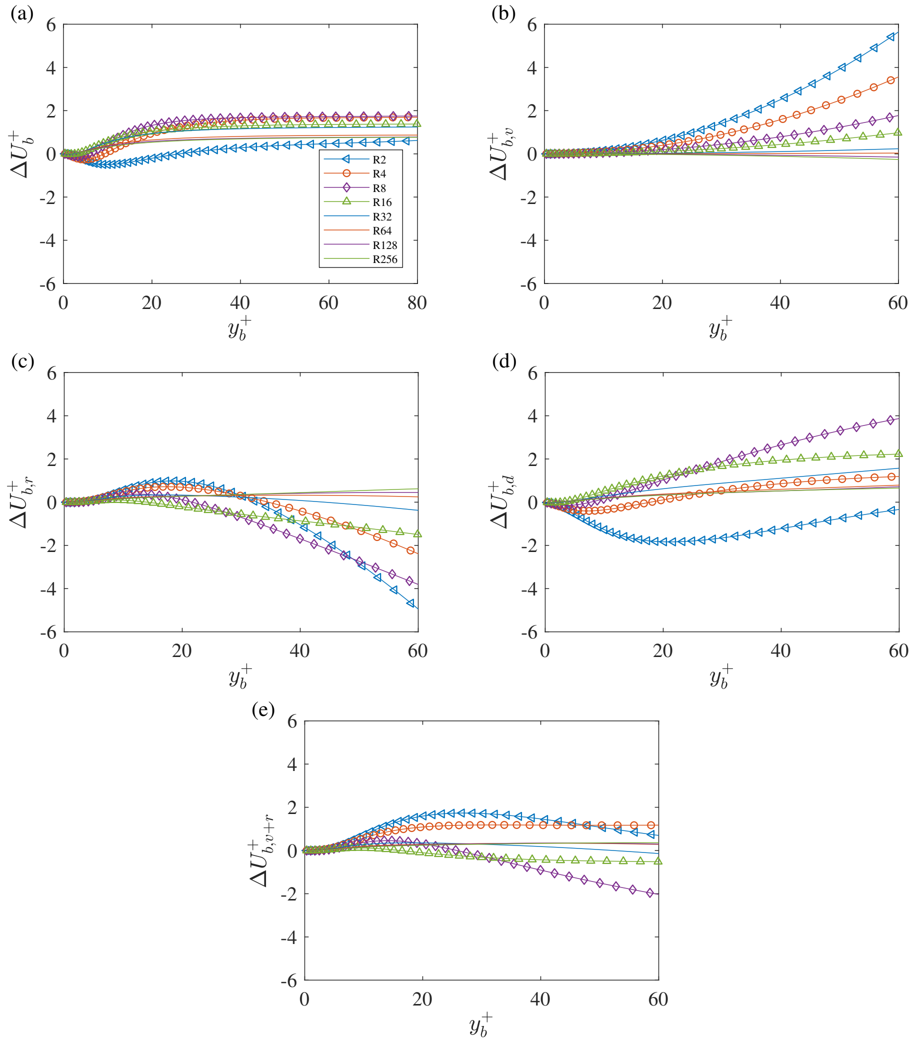

Figure 7: (a) Generalized roughness functions ΔU_b^+ for $0 < y_b^+ < 80$. (b) The viscous contributions. (c) The turbulent contributions. (d) The dispersive contributions. (e) The summation of viscous and turbulent contributions.

For the flows considered in this study, integrating twice leads to

$$(U_b^+ - U_{s,b}^+) = \left(y_b^+ - \frac{Re_\tau^2}{2Re_{\tau,b}^3} y_b^{+2}\right) + \int_0^{y_b^+} \left\langle \overline{u'v'} \right\rangle_b^+ d\tilde{y}_b^+ + \int_0^{y_b^+} \langle \bar{u}''\bar{v}'' \rangle_b^+ \, d\tilde{y}_b^+. \tag{19}$$

where $F_b = u_\tau^2/h$ due to the force balance. Next, subtracting (18) from (19), we have

$$\Delta U_b^+ = \underbrace{\left(\frac{Re_\tau^2}{2Re_{\tau,b}^3} - \frac{1}{2Re_\tau}\right) y_b^{+2}}_{\Delta U_{b,v}^+} + \underbrace{\int_0^{y_b^+} \left(\overline{u'v'}_{\mathrm{pc}}^+ - \left\langle \overline{u'v'} \right\rangle_b^+\right) d\tilde{y}_b^+}_{\Delta U_{b,r}^+} \underbrace{- \int_0^{y_b^+} \langle \bar{u}''\bar{v}'' \rangle_b^+ \, d\tilde{y}_b^+}_{\Delta U_{b,d}^+}. \tag{20}$$

Equation (20) serves as a decomposition of the generalized roughness function. The terms on the right-hand side are due to viscous stress, Reynolds stress, and dispersive stress and are denoted as $\Delta U_{b,v}^+$, $\Delta U_{b,r}^+$, $\Delta U_{b,d}^+$, i.e., $\Delta U_b^+ = \Delta U_{b,v}^+ + \Delta U_{b,r}^+ + \Delta U_{b,d}^+$. It should be noted that the contribution from the viscous stress arises due to the asymmetric wall boundary conditions and the term will vanish when $Re_{\tau,b} = Re_\tau$.

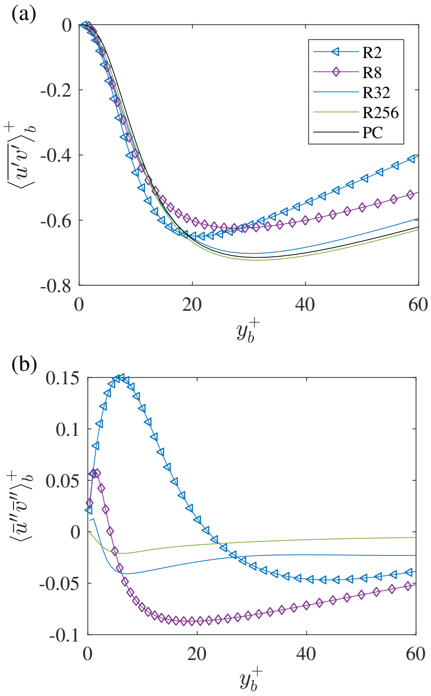

Figure 8: (a) Reynolds stress $\langle \overline{u'v'} \rangle$ profiles for selected cases. (b) Same as (a) but for the dispersive stress $\langle \bar{u}''\bar{v}'' \rangle$. The normalization is based on the local wall units.

Figure 7 (a) shows the generalized roughness functions as a function of y_b^+. It remains nearly constant for $y_b^+ > 30$, reducing to its conventional definition. However, in case R2, the log law slope of the mean flow differs from that of a plane channel, resulting in a continued increase of the generalized roughness function with y_b^+ beyond the buffer layer. Figures 7 (b, c, d) isolate the contributions of viscous, turbulent, and dispersive stresses to the generalized roughness function. Here, we concentrate on the wall layer, excluding data beyond $y_b^+ = 60$. Several observations emerge. The viscous term $\Delta U_{b,v}^+$ is positive in R2-64 and contributes to drag increase. In these cases, the term is an increasing function of y_b^+ and a decreasing function of l_b^+. In R128 and R256, $\Delta U_{b,v}^+$ is negative and therefore contributes to drag reduction. The behavior of the turbulent term $\Delta U_{b,r}^+$ is more intricate. In R2-32, the term increases as a function of y_b^+ in the sublayer and then decreases as a function of y_b^+. In R64-256, the term gradually increases as a function of y_b^+ and is slightly positive at $y_b^+ = 60$. The dispersive stress term is even more intricate. It is negative in R2, contributing to drag reduction. In R4 and R8, the term is negative near the wall but quickly becomes positive in the log layer, contributing to drag reduction near the wall and drag increase further away. In R16-256, the term stays positive, and its magnitude decreases as l_b^+ decreases. Comparing $\Delta U_{b,v}^+$ and $\Delta U_{b,r}^+$, we see that they have opposite signs outside the wall layer. Also, comparing the two terms to $\Delta U_{b,d}^+$, we see that the two terms significantly exceed $\Delta U_{b,d}^+$ outside the wall layer. This leads us to define $\Delta U_{b,v+r}^+ = \Delta U_{b,v}^+ + \Delta U_{b,r}^+$. Figure 7 (e) illustrates $\Delta U_{b,v+r}^+$. The term is comparable to $\Delta U_{b,d}^+$. In R2-16, $\Delta U_{b,v+r}^+$ and $\Delta U_{b,d}^+$ generally exhibit opposite signs, resulting in a $|\Delta U_b^+|$ smaller than $|\Delta U_{b,v+r}^+|$ and $|\Delta U_{b,d}^+|$. Conversely, in R32-256, $\Delta U_{b,v+r}^+$ closely approaches zero, and $\Delta U_b^+ \approx \Delta U_{b,d}^+$. Thus, we conclude that the drag increase in R128 and R256 arises from the subdued $\Delta U_{b,v+r}^+$ alongside a non-zero $\Delta U_{b,d}^+$.

To gain an understanding of the turbulent and dispersive stress contributions, we plot $\langle \overline{u'v'} \rangle$ and $\langle \bar{u}''\bar{v}'' \rangle$ as a functions of y_b^+ in Figures 8 (a, b). Comparing R2 and the plane channel flow, $\langle \overline{u'v'} \rangle$ in R2 is slightly smaller than that in a plane channel in the wall layer for $y^+ \lesssim 20$ and larger for $y^+ \gtrsim 20$. This explains the initial increase of $\Delta U_{b,r}^+$ in the wall layer and its subsequent decrease further away. As l_b^+ decreases, the Reynolds shear stress converges to the plane channel value, leading to a vanishing $\Delta U_{b,r}^+$. The dispersive stress in R2 is positive near the wall for $y^+ \lesssim 20$ and negative above, contributing to a decreasing $\Delta U_{b,d}$ in the wall layer and an increasing $\Delta U_{b,d}$ outside. As l_b^+ decreases, the region within which $\langle \bar{u}''\bar{v}'' \rangle$ stays positive narrows, leading to a positive $\Delta U_{b,d}^+$ in R32 and R256.

4.3. Secondary flows

Having identified that the non-zero dispersive stress or the secondary flows are responsible for drag increase at the anticipated hydraulically smooth limit, we now study the behaviors of the secondary flows as we vary the wavelength of the surface pattern.

Figure 9 shows the contours of $\bar{u}_b^+$ in the spanwise/wall-normal plane. We see secondary flows that manifest as counter-rotating vortices. In R2 and R4, the secondary vortices bring fluid from the slip-wall regions to the no-slip-wall regions. This gives rise to a positive and negative wall-normal velocity above the slip and the no-slip walls, which in turn gives rise to a positive $\langle \bar{u}''\bar{v}'' \rangle$. In R8 and R16, the secondary vortices bring fluid from the no-slip-wall regions to the slip-wall regions, giving rise to negative and positive wall-normal velocities above the slip- and no-slip wall regions and a negative $\langle \bar{u}''\bar{v}'' \rangle$. In R32 and R128, the secondary flows are confined in the viscous layer and are hard to recognize in the figure.

The wall-normal location where $\langle \bar{v}''\bar{v}'' \rangle$ attains its maximum measures the sizes of the secondary flows (Forooghi et al., 2020). Figure 10 shows the secondary flow size as a function of l_b^+. We see that the size of the secondary flows H_b^+ does not change monotonically as a function of l_b^+: H_b^+ decreases from about 19 in R2 to about 5.6 in R4. It then increases to about 13 in R8 and decreases to about 1.1 in R32. Further decreasing l_b^+ has no effect on H_s^+ and its value remains about 1.1 in R32-256.

Lastly, we examine the flow above the no-slip-wall regions and the slip-wall regions respectively to identify which region is responsible for the observed drag increase in the anticipated hydraulically smooth regime. Figure 11 shows the mean flow as a function of the wall-normal coordinate at a few z locations. We have subtracted the velocity at the wall so that the discussion focuses on the roughness function ΔU_b^+. The plane channel result is included here for comparison purposes. We see that the profiles above the no-slip wall regions are above the plane channel profile whereas the profiles above the slip-wall regions are below the plane channel profile. As l_b^+ decreases, profiles above

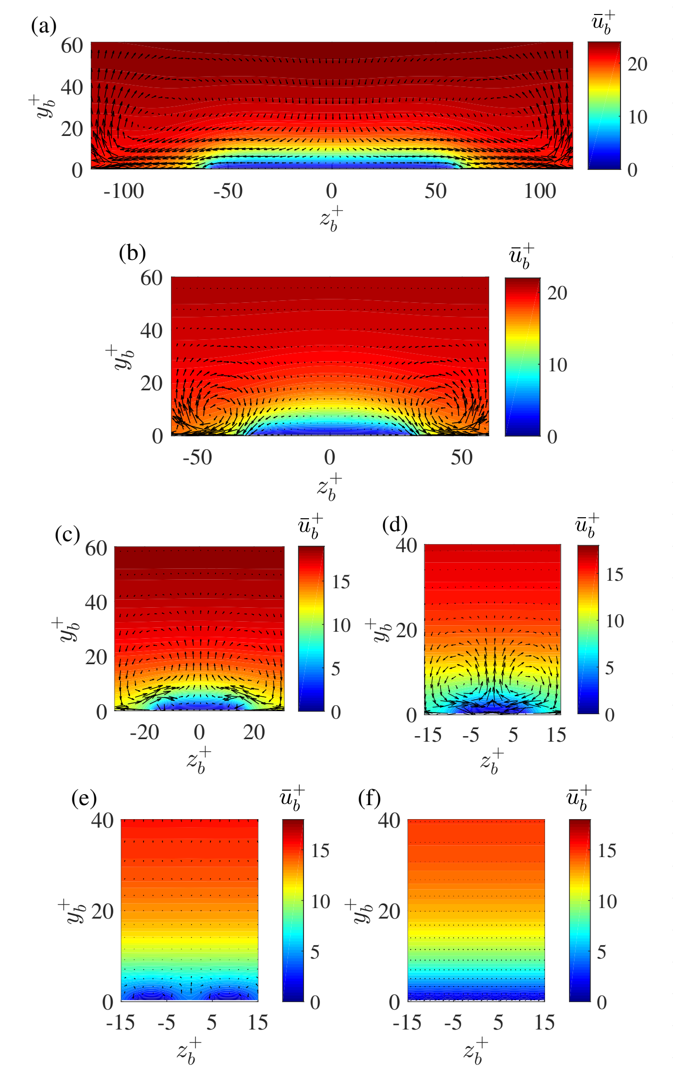

Figure 9: Contours of the temporally averaged streamwise velocity $\bar{u}$ in the transverse-wall-normal plane. The normalization is based on the wall units at the bottom wall. The vectors indicate the in-plane motions $(\bar{v}, \bar{w})$. We show only part of the domain. The mean flow repeats itself in the transverse direction. The origin of the spanwise coordinate is placed at the center of the no-slip patch. The cases are (a) R2, (b) R4, (c) R8, (d) R16, (e) R32, (f) R128.

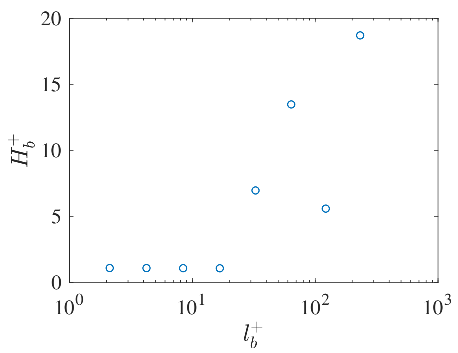

Figure 10: The size of the secondary flow structures as a function of pattern wavelength in bottom wall units. Here, the size of the secondary flows is measured by the wall-normal location where $\langle \bar{v}''\bar{v}'' \rangle$ peaks.

both the no-slip wall regions and the slip-wall regions converge to the plane channel profile. However, the profiles above the slip wall regions converge to the plane channel profile more slowly than the profiles above the no-slip wall regions. Hence, we conclude that the negative ΔU_b^+ in R128 and R256 is due to the flow above the slip wall.

5. The effect of spanwise slip

In §4, we poist that the secondary flows in the viscous layer are responsible for the drag increase at the hydraulically smooth limit. If that were right, reducing/preventing secondary flows in the viscous layer would reduce/prevent the drag increase at the hydraulically smooth limit. To that end, we impose no-slip in the spanwise direction in cases X4, X16, and X128. This will effectively suppress motions in the spanwise direction very close to the wall, leading to a reduction of secondary motions in the viscous layer. In this section, we compare these modified X cases to their counterpart R cases, examining the resulting behaviors of the mean flow. We note that the method of separating spanwise and streamwise slip has a long history and dates back to Min and Kim (2004). In this context here, since the intended application is the wall-shear-stress-dependent slip at the molecular scale, it is particularly relevant to separate the slip in the streamwise and the spanwise directions, as the wall-shear stresses in these two directions are distinctly different.

Figure 12 shows the mean flow results. We see from Figure 12 (a) that preventing spanwise slip results in higher velocities in the log layer for the X cases compared to the R cases. Figure 12 (c) shows the slip velocity at the wall. Due to the reduced skin friction in the X cases, the spanwise length scale $l_b^+ = lu_{\tau,b}/\nu$ in these cases is slightly smaller than that in the R cases. Consequently, the symbols representing the X cases are positioned slightly to the left of those representing the R cases in Figure 12 (c). We see that imposing a no-slip condition in the spanwise direction gives rise to a slightly higher slip velocity in X4 than in R4 but has essentially no effect on the slip velocity in X/R16 and X/R128. Figure 12 (b) shows $U_b^+ - U_{s,b}^+$ and (d) illustrates the roughness function ΔU_b^+. The roughness functions in the X cases are noticeably smaller than those in the counterpart R cases. In particular, $U_b^+ - U_{s,b}^+$ in X128 already follows closely the profile in a plane channel. Figure 13 shows $U_{s,b}^+ - \Delta U_b^+$, $\tau_{w,b}/u_\tau^2$, U_{bulk} and C_f. The four provide a measure of the overall drag reduction/increase on the bottom wall. We see reduced drag in the X cases compared to their R counterparts. Of particular significance, the roughness function is close to 0 in X128, i.e., $U_{s,b}^+ - \Delta U_b^+ \approx U_{s,b}^+$. Hence, X128 achieves a state akin to the hypothesized hydraulically smooth limit.

Next, we repeat the exercise in §4 and analyze the budget of the generalized roughness function. The objective is to identify the processes responsible for the differences between the X and the R cases. Figure 14 shows the viscous, turbulent, and dispersive stress contributions to the generalized roughness function. From Figure 14 (a), we see that imposing no-slip in the spanwise direction leads to increased $\Delta U_{b,v}^+$ in the X cases than in

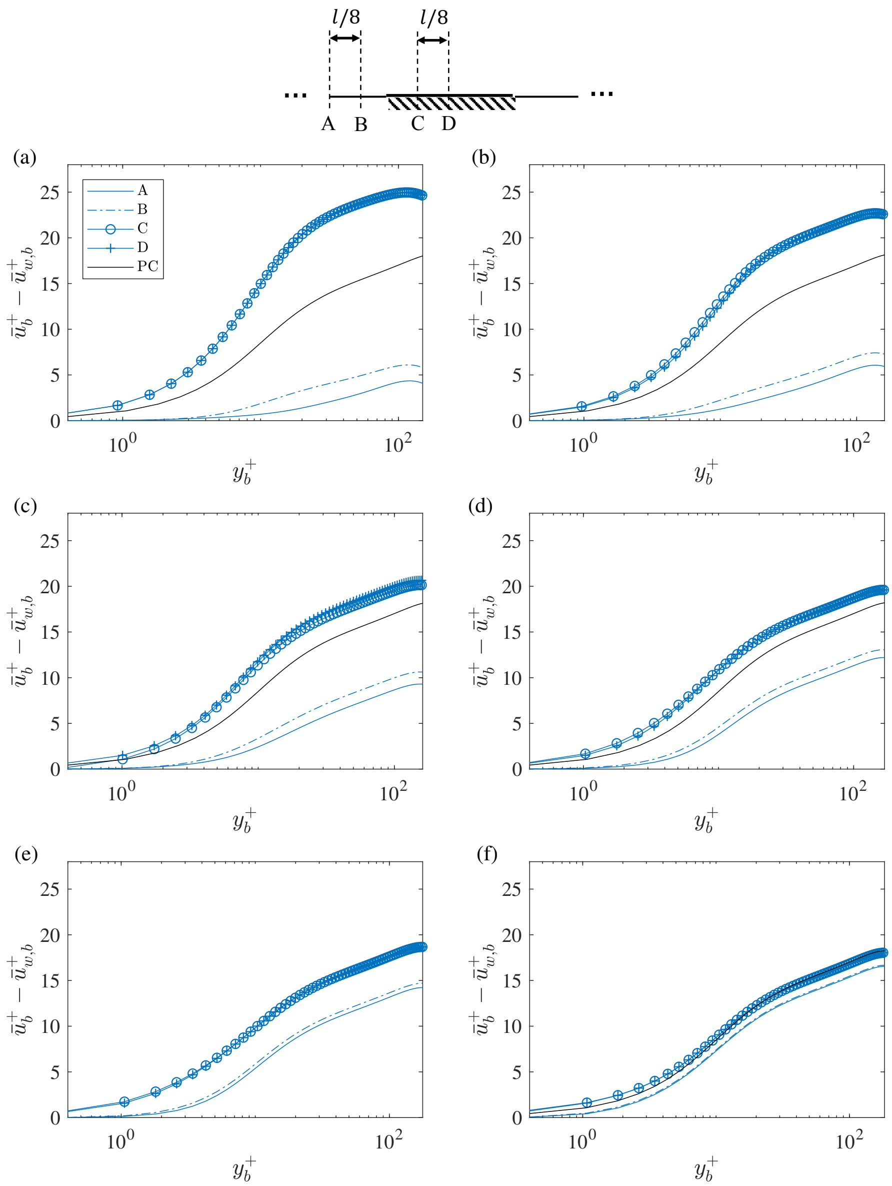

Figure 11: Mean velocity at constant z locations as indicated in the sketch. A and D are at the centers of the slip-wall and no-slip-wall regions. B and C are $l/8$ from A and D, respectively. The cases are (a)R2, (b)R4, (c)R8, (d)R16, (e)R32, (f)R128.

the R cases. In particular, $\Delta U^+_{b,v}$ is negative in R128, contributing to drag reduction, but positive in X128, contributing to drag increase. Examining the turbulent contribution $\Delta U^+_{b,r}$ in Figure 14 (b), we observe minimal impact on this term when l_b^+ is large. Specifically, $\Delta U^+_{b,r}$ in R4 and X4 are similar, as do R16 and X16. However, a distinct difference emerges between X128 and R128. In X128, $\Delta U^+_{b,r}$ is negative, whereas in R128, it is positive. Finally, Figure 14 (c) presents $\Delta U^+_{b,d}$. Our expectation that a no-slip condition would impede secondary flows in the viscous layer, thereby reducing $\Delta U^+_{b,d}$, is confirmed. The X cases exhibit a notable reduction in the magnitude of $\Delta U^+_{b,d}$ compared to the R cases.

The results in Figure 14 indicate that the subdued secondary flows are responsible for the reduced skin friction coefficient in the X cases when compared to the counterpart R cases. To gain further insights into the response of the secondary flows to the spanwise wall boundary condition, we revisit the analysis from §4.3. Specifically, we examine the velocity profiles above the (streamwise) slip wall regions and the (streamwise) no-slip wall regions. Figure 15 shows the results. At smaller l_b^+, the imposition of a no-slip condition in the spanwise direction leads to higher velocities above both the no-slip regions and the slip regions. This results in a slower convergence of the profiles above the no-slip regions to the plane channel profile and a faster convergence of the profiles above the slip regions. These effects together contribute to the reduced drag forces in the X cases than in the R cases.

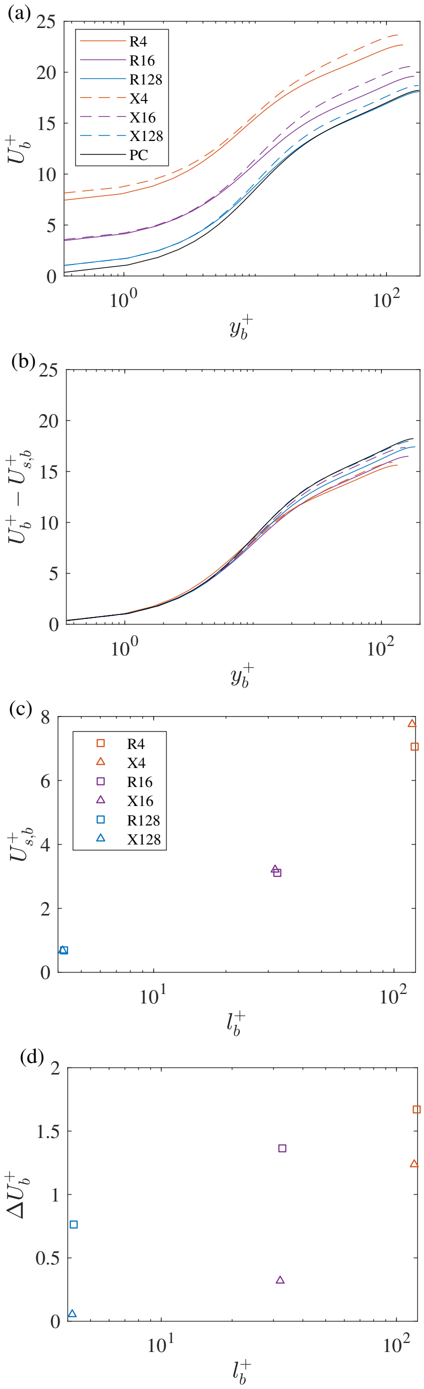

Figure 12: (a) Mean velocity profiles in X4, X16, and X128. The results of R4, R16, and R128 are included here for comparison purposes. (b) $U_b^+ - U_{s,b}^+$ as a function of the wall-normal coordinate. The legend is the same as in (a). (c) Slip velocities as a function of the spanwise length scale l_b^+ for R/X4, R/X16, and R/X128. We use squares for the R cases and triangles for the X cases. (d) Roughness function as a function of l_b^+. The legend is the same as in (c).

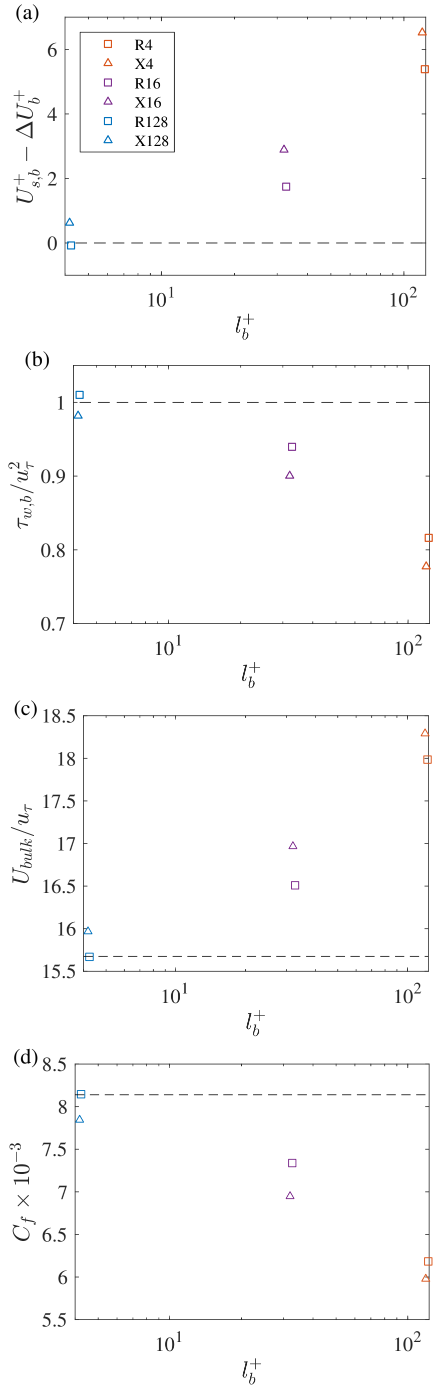

Figure 13: (a) $U_{s,b}^+ - \Delta U_b^+$ as a function of l_b^+ for R/X4, R/X16, and R/X128. (b) Bottom wall shear stress. (c) Bulk velocity. (d) Skin friction coefficient. Again, the square symbols are for R cases, and the triangle symbols are for X cases. The plane channel results are marked by the dashed lines.

6. Conclusions

We conduct DNSs of flow over surfaces with spanwise alternating strips of slip and no-slip walls. The size of the repeating surface pattern is varied from 1.5 times the half channel height to 2 viscous units, reaching the anticipated hydraulically

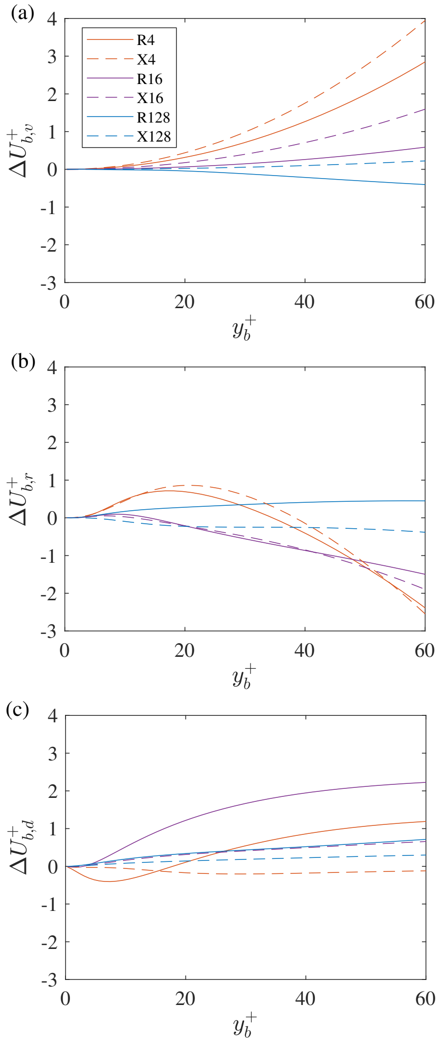

Figure 14: (a) Contributions to the generalized roughness function in X/R4, X/R16, and X/R128. (a) The viscous contributions (b) The turbulent contributions. (c) The dispersive contributions.

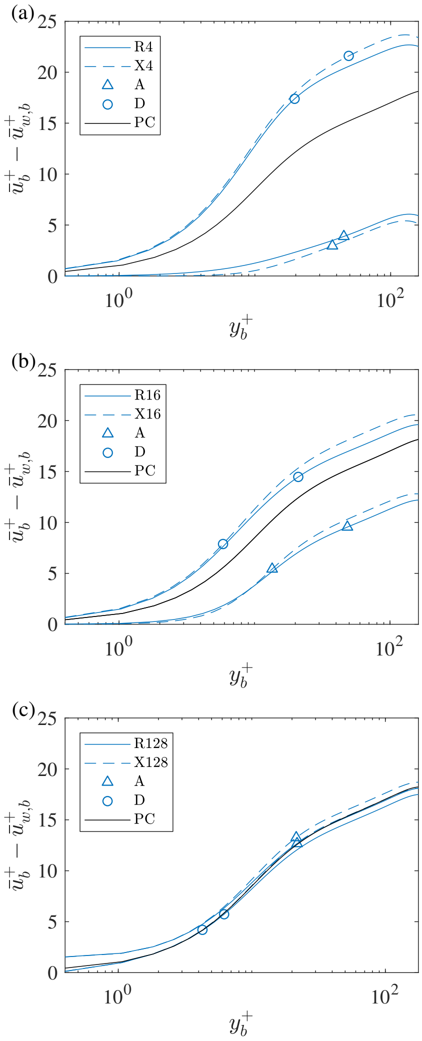

Figure 15: Mean streamwise velocity at some z locations. The symbols indicate the spanwise location, see Figure 11. The normalization is by the local wall units. The cases are (a) R/X4, (b) R/X16, (c) R/X128.

smooth limit. While this limit has little practical relevance to riblets and grooves, it is relevant to the recently found slip at the molecular level. The slip wall induces a slip velocity U_s at the wall, which contributes to drag reduction. The spanwise heterogeneity in the surface gives rise to secondary flows. These secondary flows lead to a downward shift in the log region ΔU, which contributes to drag increase. The sum of the two, i.e., $-U_s + \Delta U$ measures whether the surface increases or reduces drag, with a positive value indicating drag increase and a negative value indicating drag reduction. The common expectation is that a mixture of slip and no-slip walls should lead to drag reduction. At worst, the flow reduces to that in a plane channel at the hydraulically smooth limit when l approaches 0. However, we see a drag increase at the anticipated hydraulically smooth limit. At that limit, the slip velocity is essentially 0 but the roughness function is slightly positive. According to the grid convergence study in Türk et al. (2014), the present estimate is an underestimate of the drag force and therefore the true drag increase can only be more significant. In order to identify the mechanisms that are responsible for this drag increase and to overcome the difficulty of measuring the roughness function when the log region is narrow and hard to define, we derive a Navier-Stokes-based decomposition of the generalized roughness function. This decomposition contains a viscous contribution, a turbulent contribution, and a dispersive contribution. The analysis shows that a non-zero dispersive contribution in the viscous layer is responsible for the drag increase at the anticipated hydraulically smooth limit. Further analysis of the mean flow data indicates that the flow above the slip-wall regions is the culprit of the drag increase at the anticipated hydraulically smooth limit. To further verify this conclusion, we follow Min and Kim (2004); Fukagata et al. (2006) and impose the no-slip boundary condition in the spanwise direction. Imposing no-slip in the spanwise direction reduces the strength of secondary flows in the viscous layer. If the drag increase at the anticipated hydraulically smooth limit is truly a result of secondary flows, imposing no-slip in the spanwise direction should effectively reduce/remove that drag increase. This expectation bears out in

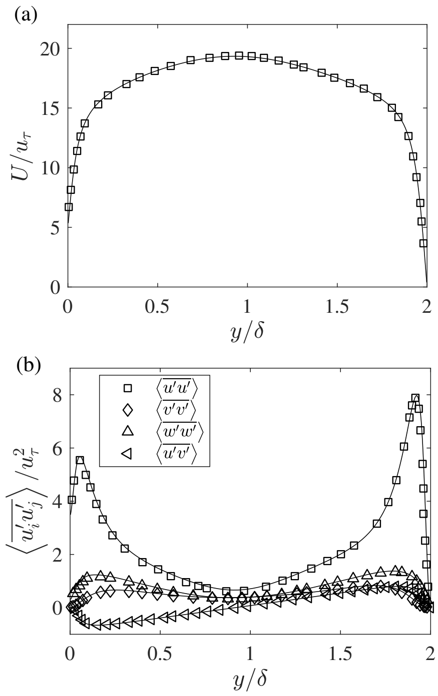

Figure A.16: A comparison between the present DNS (lines) and the "30μm – 30μm" case (symbols) in Martell et al. (2009). (a) Mean streamwise velocity, (b) Reynolds stresses.

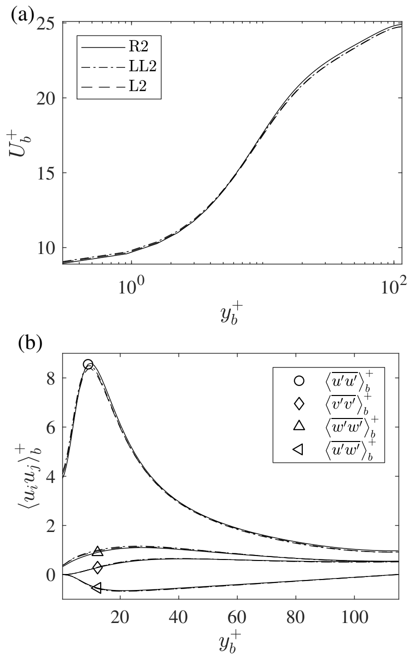

Figure A.17: (a) Mean streamwise velocity profiles for R2/LL2/L2. (b) Same as (a) but for Reynolds stress profiles and the same legend as in (a) is used.

our DNSs. In all, the results of this study, which are conservative, suggest that the anticipated hydraulically smooth limit might not exist for some surfaces.

Acknowledgements

HX acknowledges the Ocean University of China. XY acknowledges NSF EAGER 2231037 and NSF Grant 2241730.

Appendix A. Further details

To further validate the DNS code, we replicate the results in Martell et al. (2009). Figures A.16 (a,b) show the comparison. We see a good agreement between the present DNS and the results in Martell et al. (2009). This serves as a further validation. We conducted a domain convergence study for R2, i.e., where we see the largest difference between the bottom and top wall shear stresses. The mean streamwise velocity and dominated Reynolds stresses are shown in Figures A.17 (a,b). We see good agreements from R2, LL2, and L2, with less than 1% difference. Hence, the present domain size is adequate. The same is true for other cases. Figures A.18 (a,b) compare R8 and L8, and we see a good agreement between the two DNSs.

We show the mean momentum budget for all the R cases in Figure A.19. We see that the total stresses follow the expected linear function, and therefore the flow is statistically converged.

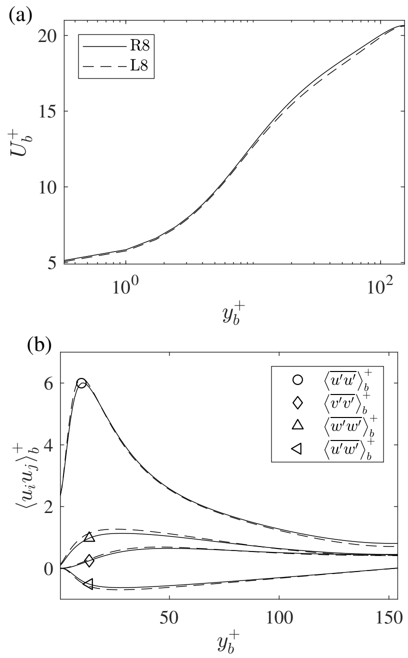

Figure A.18: (a) Mean streamwise velocity profiles for R8/L8. (b) Same as (a) but for Reynolds stress profiles and the same legend as in (a) is used.

References

Adrian, R., 2007. Hairpin vortex generation in wall turbulence. Phys. Fluids 19.

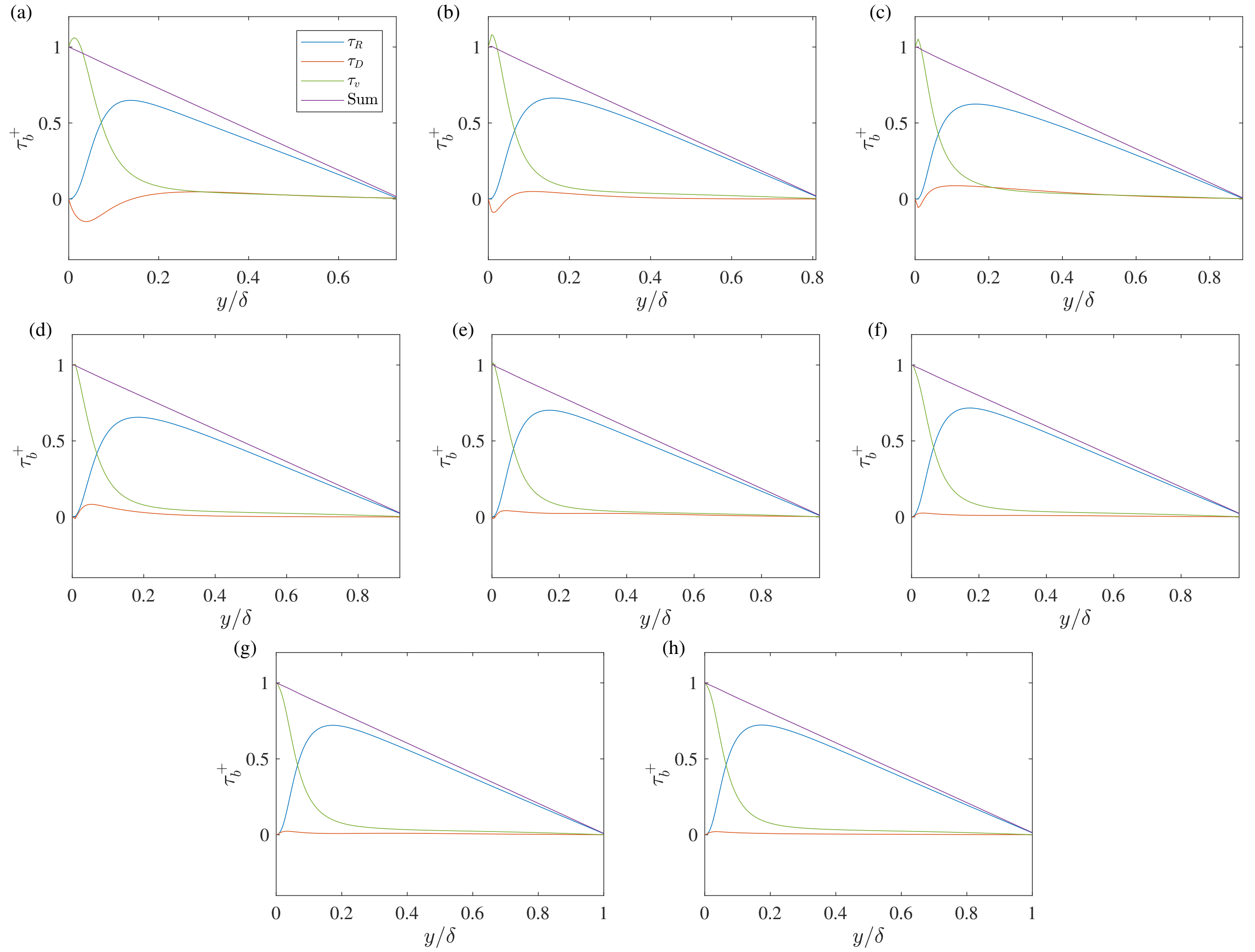

Figure A.19: The mean momentum budget balance. The cases are (a) R2, (b) R4, (c) R8, (d) R16, (e) R32, (f) R64, (g) R128, (h) R256. Here, τ_R is the Reynolds stress, τ_D is the dispersive stress, and τ_v is the viscous stress.

Altland, S., Zhu, X., McClain, S., Kunz, R., Yang, X., 2022. Flow in additively manufactured super-rough channels. Flow 2, E19.

Anderson, W., Barros, J.M., Christensen, K.T., Awasthi, A., 2015a. Numerical and experimental study of mechanisms responsible for turbulent secondary flows in boundary layer flows over spanwise heterogeneous roughness. J. Fluid Mech. 768, 316–347.

Anderson, W., Li, Q., Bou-Zeid, E., 2015b. Numerical simulation of flow over urban-like topographies and evaluation of turbulence temporal attributes. J. Turbul. 16, 809–831.

Anderson, W., Yang, J., Shrestha, K., Awasthi, A., 2018. Turbulent secondary flows in wall turbulence: vortex forcing, scaling arguments, and similarity solution. Environ. Fluid Mech. 18, 1351–1378.

Barros, J.M., Christensen, K.T., 2014. Observations of turbulent secondary flows in a rough-wall boundary layer. J. Fluid Mech. 748.

Bechert, D., Bruse, M., Hage, W.v., Van der Hoeven, J.T., Hoppe, G., 1997. Experiments on drag-reducing surfaces and their optimization with an adjustable geometry. J. Fluid Mech. 338, 59–87.

Belcher, S., Jerram, N., Hunt, J., 2003. Adjustment of a turbulent boundary layer to a canopy of roughness elements. J. Fluid Mech. 488, 369–398.

Bose, S.T., Park, G.I., 2018. Wall-modeled large-eddy simulation for complex turbulent flows. Ann. Rev. Fluid Mech. 50, 535–561.

Bou-Zeid, E., Meneveau, C., Parlange, M., 2005. A scale-dependent lagrangian dynamic model for large eddy simulation of complex turbulent flows. Phys. Fluids 17, 025105.

Carré, A., Mittal, K.L., 2009. Superhydrophobic surfaces. CRC Press.

Chen, P.E., Zhu, X., Shi, Y., Yang, X.I., 2023. Quantifying uncertainties in direct-numerical-simulation statistics due to wall-normal numerics and grids. Phys. Rev. Fluids 8, 074602.

Chester, S., Meneveau, C., Parlange, M.B., 2007. Modeling turbulent flow over fractal trees with renormalized numerical simulation. J. Comput. Phys. 225, 427–448.

Choi, H., Moin, P., Kim, J., 1993. Direct numerical simulation of turbulent flow over riblets. J. Fluid Mech. 255, 503–539.

Chung, D., Monty, J.P., Hutchins, N., 2018. Similarity and structure of wall turbulence with lateral wall shear stress variations. J. Fluid Mech. 847, 591–613.

Coceal, O., Thomas, T., Castro, I., Belcher, S., 2006. Mean flow and turbulence statistics over groups of urban-like cubical obstacles. Boundary-Layer Meteorol. 121, 491–519.

Elnahhas, A., Johnson, P.L., 2022. On the enhancement of boundary layer skin friction by turbulence: an angular momentum approach. J. Fluid Mech. 940, A36.

Endrikat, S., Modesti, D., MacDonald, M., García-Mayoral, R., Hutchins, N., Chung, D., 2021. Direct numerical simulations of turbulent flow over various riblet shapes in minimal-span channels. Flow Turbul. Combust. 107, 1–29.

Fairhall, C., Abderrahaman-Elena, N., García-Mayoral, R., 2019. The effect of slip and surface texture on turbulence over superhydrophobic surfaces. J. Fluid Mech. 861, 88–118.

Fairhall, C., García-Mayoral, R., 2018. Spectral analysis of the slip-length model for turbulence over textured superhydrophobic surfaces. Flow Turbul. Combust. 100, 961–978.

Finnigan, J., Ayotte, K., Harman, I., Katul, G., Oldroyd, H., Patton, E., Poggi, D., Ross, A., Taylor, P., 2020. Boundary-layer flow over complex topography. Boundary-Layer Meteorol. 177, 247–313.

Flack, K.A., Schultz, M.P., Rose, W.B., 2012. The onset of roughness effects in the transitionally rough regime. Int. J. Heat Fluid Flow 35, 160–167.

Forooghi, P., Yang, X.I., Abkar, M., 2020. Roughness-induced secondary flows in stably stratified turbulent boundary layers. Phys. Fluids 32, 105118.

Fukagata, K., Iwamoto, K., Kasagi, N., 2002. Contribution of reynolds stress distribution to the skin friction in wall-bounded flows. Phys. Fluids 14, L73–L76.

Fukagata, K., Kasagi, N., Koumoutsakos, P., 2006. A theoretical prediction of friction drag reduction in turbulent flow by superhydrophobic surfaces. Phys. Fluids 18.

García-Mayoral, R., Jimenez, J., 2011. Hydrodynamic stability and breakdown of the viscous regime over riblets. J. Fluid Mech. 678, 317–347.

García-Mayoral, R., Jiménez, J., 2012. Scaling of turbulent structures in riblet channels up to re$\tau \approx 550$. Phys. Fluids 24.

Hansen, C., Yang, X.I., Abkar, M., 2023. Data-driven dynamical system models of roughness-induced secondary flows in thermally stratified turbulent boundary layers. J. Fluids Eng. 145, 061102.

Hong, J., Katz, J., Meneveau, C., Schultz, M.P., 2012. Coherent structures and associated subgrid-scale energy transfer in a rough-wall turbulent channel flow. J. Fluid Mech. 712, 92–128.

Hong, J., Katz, J., Schultz, M.P., 2011. Near-wall turbulence statistics and flow structures over three-dimensional roughness in a turbulent channel flow. J. Fluid Mech. 667, 1–37.

Jelly, T., Jung, S., Zaki, T., 2014. Turbulence and skin friction modification in channel flow with streamwise-aligned superhydrophobic surface texture. Phys. Fluids 26, 095102.

JHU-LESGO, 2019. A parallel pseudo-spectral large-eddy simulation code. https://lesgo.me.jhu.edu.

Lee, S.J., Lee, S.H., 2001. Flow field analysis of a turbulent boundary layer over a riblet surface. Exp. Fluids. 30, 153–166.

Ma, R., Alamé, K., Mahesh, K., 2021. Direct numerical simulation of turbulent channel flow over random rough surfaces. J. Fluid Mech. 908, A40.

MacDonald, M., Chung, D., Hutchins, N., Chan, L., Ooi, A., García-Mayoral, R., 2017. The minimal-span channel for rough-wall turbulent flows. J. Fluid Mech. 816, 5–42.

Martell, M.B., Perot, J.B., Rothstein, J.P., 2009. Direct numerical simulations of turbulent flows over superhydrophobic surfaces. J. Fluid Mech. 620, 31–41.

Martell, M.B., Rothstein, J.P., Perot, J.B., 2010. An analysis of superhydrophobic turbulent drag reduction mechanisms using direct numerical simulation. Phys. Fluids 22, 065102.

Martin, S., Bhushan, B., 2016. Fluid flow analysis of continuous and segmented riblet structures. Rsc Advances 6, 10962–10978.

Mednjoun, T., Vanderwel, C., Ganapathisubramani, B., 2018. Characteristics of turbulent boundary layers over smooth surfaces with spanwise heterogeneities. J. Fluid Mech. 838, 516–543.

Mejia-Alvarez, R., Barros, J.M., Christensen, K.T., 2013. Structural attributes of turbulent flow over a complex topography. Coherent Flow Structures at Earth's Surface , 25–41.

Min, T., Kim, J., 2004. Effects of hydrophobic surface on skin-friction drag. Phys. Fluids 16, L55–L58.

Modesti, D., Endrikat, S., Hutchins, N., Chung, D., 2021. Dispersive stresses in turbulent flow over riblets. J. Fluid Mech. 917.

Moser, R.D., Kim, J., Mansour, N.N., 1999. Direct numerical simulation of turbulent channel flow up to re τ= 590. Phys. Fluids 11, 943–945.

Neuhauser, J., Schäfer, K., Gatti, D., Frohnapfel, B., 2022. Simulation of turbulent flow over roughness strips. J. Fluid Mech. 945, A14.

Nikuradse, J., 1933. Laws of flow in rough pipes. national advisory committee for aeronautics. NACA Technical Memorandum, NACA Technical Memorandum 1292, 60–68.

Nozarian, S., Abkar, M., Forooghi, P., 2024. An analysis of drag reduction using spanwise forcing on rough walls. Int J Heat Fluid Flow 106, 109306.

Park, H., Park, H., Kim, J., 2013. A numerical study of the effects of superhydrophobic surface on skin-friction drag in turbulent channel flow. Phys. Fluids 25, 110815.

Ramos-Alvarado, B., Kumar, S., Peterson, G., 2016. Hydrodynamic slip length as a surface property. Physical Review E 93, 023101.

Rastegari, A., Akhavan, R., 2015. Effect of interface curvature on superhydrophobic drag reduction, in: APS Division of Fluid Dynamics Meeting Abstracts, pp. R18–002.

Renard, N., Deck, S., 2016. A theoretical decomposition of mean skin friction generation into physical phenomena across the boundary layer. J. Fluid Mech. 790, 339–367.

Salesky, S.T., Calaf, M., Anderson, W., 2022. Unstable turbulent channel flow response to spanwise-heterogeneous heat fluxes: Prandtl's secondary flow of the third kind. J. Fluid Mech. 934, A46.

Schlichting, H., Gersten, K., 1979. Boundary-layer theory. macgraw hill. New York .

Schlichting, H., Kestin, J., Street, R.L., 1980. Boundary-layer theory .

Snyder, J.C., Thole, K.A., 2020. Tailoring surface roughness using additive manufacturing to improve internal cooling. J. Turbomach. 142, 071004.

Suzuki, Y., Kasagi, N., 1994. Turbulent drag reduction mechanism above a riblet surface. AIAA journal 32, 1781–1790.

Thompson, P.A., Troian, S.M., 1997. A general boundary condition for liquid flow at solid surfaces. nature 389, 360–362.

Tomlinson, S.D., Peaudecerf, F.J., Temprano-Coleto, F., Gibou, F., Luzzatto-Fegiz, P., Jensen, O.E., Landel, J.R., 2023. A model for slip and drag in turbulent flows over superhydrophobic surfaces with surfactant. Int J Heat Fluid Flow 103, 109171.

Türk, S., Daschiel, G., Stroh, A., Hasegawa, Y., Frohnapfel, B., 2014. Turbulent flow over superhydrophobic surfaces with streamwise grooves. J. Fluid Mech. 747, 186–217.

Vanderwel, C., Ganapathisubramani, B., 2015. Effects of spanwise spacing on large-scale secondary flows in rough-wall turbulent boundary layers. J. Fluid Mech. 774.

Volino, R.J., Schultz, M.P., 2018. Determination of wall shear stress from mean velocity and reynolds shear stress profiles. Phys. Rev. Fluids 3, 034606.

Wangsawijaya, D.D., Baidya, R., Chung, D., Marusic, I., Hutchins, N., 2020. The effect of spanwise wavelength of surface heterogeneity on turbulent secondary flows. J. Fluid Mech. 894, A7.

Willingham, D., Anderson, W., Christensen, K.T., Barros, J.M., 2014. Turbulent boundary layer flow over transverse aerodynamic roughness transitions: induced mixing and flow characterization. Phys. Fluids 26, 025111.

Wong, J., Camobreco, C., García-Mayoral, R., Hutchins, N., Chung, D., 2024. A viscous vortex model for predicting the drag reduction of riblet surfaces. Journal of Fluid Mechanics 978, A18.

Yang, J., Anderson, W., 2018. Numerical study of turbulent channel flow over surfaces with variable spanwise heterogeneities: topographically-driven secondary flows affect outer-layer similarity of turbulent length scales. Flow Turbul. Combust. 100, 1–17.

Yang, X., Sadique, J., Mittal, R., Meneveau, C., 2015. Integral wall model for large eddy simulations of wall-bounded turbulent flows. Phys. Fluids 27, 025112.

Yang, X., Xu, H., Huang, X., Ge, M.W., 2019. Drag forces on sparsely packed cube arrays. J. Fluid Mech. 880, 992–1019.

Yang, X., Zhang, W., Yuan, J., Kunz, R.F., 2023. In search of a universal rough wall model. J. Fluids Eng. , 1–30.

Yang, X.I., Hong, J., Lee, M., Huang, X.L., 2021. Grid resolution requirement for resolving rare and high intensity wall-shear stress events in direct numerical simulations. Phys. Rev. Fluids 6, 054603.

Yang, X.I., Park, G.I., Moin, P., 2017. Log-layer mismatch and modeling of the fluctuating wall stress in wall-modeled large-eddy simulations. Phys. Rev. Fluids 2, 104601.

Yao, J., Chen, X., Hussain, F., 2018. Drag control in wall-bounded turbulent flows via spanwise opposed wall-jet forcing. J. Fluid Mech. 852, 678–709.

Yong, X., Zhang, L.T., 2013. Thermostats and thermostat strategies for molecular dynamics simulations of nanofluidics. The Journal of chemical physics 138.

Yoon, M., Hwang, J., Lee, J., Sung, H.J., Kim, J., 2016. Large-scale motions in a turbulent channel flow with the slip boundary condition. Int J Heat Fluid Flow 61, 96–107.

Yuan, J., Piomelli, U., 2014. Roughness effects on the reynolds stress budgets in near-wall turbulence. J. Fluid Mech. 760.

Zhang, W., Yang, X.I., Zhu, X., Wan, M., Chen, S., 2023. Asymmetric secondary flows above geometrically symmetric surface roughness. J. Fluid Mech. 970, A15.

Zhang, W., Zhu, X., Yang, X.I., Wan, M., 2022. Evidence for raupach et al.'s mixing-layer analogy in deep homogeneous urban-canopy flows. J. Fluid Mech. 944.